

Microfracture Propagation during Post-Hydraulic Fracturing Shut-in and Enhanced Gas Production from Shale*

A. Hayatdavoudi¹, A. Tavanaei², K.G. Sawant¹, F. Savage¹, and S. Salehi¹

Search and Discovery Article #41633 (2015)

Posted June 29, 2015

*Adapted from extended abstract prepared in conjunction with poster presentation at AAPG Annual Convention & Exhibition 2015, Denver, Colorado, May 31-June 3, 2015. AAPG © 2015

¹Petroleum Engineering, University of Louisiana at Lafayette, Lafayette, LA (asad.hayatdavoudi@gmail.com)

²Center for Advanced Computer Studies, UL-Lafayette, LA

Abstract

Shale gas has become an important source of energy around the globe, thus attracting many operators to engage in research on shale gas. To support the industry efforts, it is our objective to create a simple yet robust method of image analysis which would lead to better evaluation of gas bearing intervals and higher gas production from shale gas wells.

In this work, we propose an efficient method for imaging the absorbed water vapor on shale specimens. We used the SEM to generate images of the shale samples after being exposed to water vapor. We found a remarkable contrast between the sample regions where the water vapor was absorbed randomly and the unabsorbed regions. Interestingly, various types of microfractures initiated in and propagated from the regions of highly absorbed water vapor. To quantify the microfractures and the contrasting regions, we processed the SEM images. We used a segmentation algorithm to distinguish the above mentioned regions in the shale. Furthermore, dynamic thresholding and morphological concepts were applied to separate the absorbed water vapor regions from the rest. Finally, we filtered the SEM image spectrum for edge detection which was necessary for seamlessly transitioning the absorbed water vapor regions to microfractures. Specifically, (1) we map and quantify the location of capillaries activated by certain amount of moisture. (2) In earlier works (Hayatdavoudi et al., 2015; Chitila, 2014; Savage, 2014), microfractures developed in the areas of sample where moisture is absorbed. We calculate through computational processing the critical percent moisture required to activate capillaries and generate microfractures in Pierre Shale. (3) In addition, we provide values of percent area of the image of the sample occupied by microfractures. Finally (4) we present evidence as to why some areas of the sample where moisture is absorbed but do not contain microfractures.

Based on the SEM image analysis, which detect many useful attributes; the proposed method can help operators in making the best decision for shale gas prospecting. This computerized method offers the industry the following advantages: (1) Increases the speed and accuracy of the analysis of intervals with high microfracture density and identifies the microfracture types and sizes per unit mass, and (2) accurately quantifies

and separates the regions of shale where the absorbed water and the activated gas-bearing capillaries are the most abundant. These contributions could lead to the enhanced shale gas production.

Methodology

SEM Image Analysis

A digital image of a shale specimen consists of 2D data structure of pixels, each denoting exposure of gray scale in the image. In 8-bit quantization, pixels get a value in the range of 0 to 255 (2^8-1). The SEM image as a digital photo is a two-dimensional pixel array of the shale surface showing the surface and a minor depth. To detect the shale surface features in different locations and conditions, one layer gray scale image matrix is required. The acquired gray scale image consists of M by N pixels, according to the size of the image. The pixels are in the range of 0 to 255, where *peak* pixel values are close to 255 but the void spaces and dark areas are close to 0. Differences in the adjacent pixel values show the changes in the level of the grains gray scale on the shale surface. This investigation emphasizes the relative pixel values in the SEM image to detect and separate the shale moisturized regions from the other attributes of the shale surface.

Contrast Adjustment

Illumination of the image as well as location and orientation of the light affects the quality of the image; these features combine the shadows and dark grain areas in SEM images. In this work, the main objective is to separate the moist sections from the other parts of SEM image. Hence, contrast of the image should be adjusted to distinguish the darkness differences in a large distance of pixel values. Image adjustment is done by applying the suitable transformation on the gray scale matrix of the SEM image to change the contrast. The adjustment function, shown in Equation 1, γ is defined as transferring power; it specifies lightness of the transferred image. In fact, the greater transferring power ($\gamma > 1$) gives the darker final image.

$$Contrast = \left(\frac{(1 - low\ pixel\ value)}{high\ pixel\ value - low\ pixel\ value} \right)^\gamma \quad (1)$$

Edge Specification

Edge detection is a set of mathematical methods utilized in identifying parts in a digital image at which the image brightness changes abruptly. Edge detection is a helpful tool to differentiate the shale water absorbed zones from the dry zones of the image in fractured zones. The Laplacian edge detection method is used in this work, which can show the “*bold*” borders between moisture absorbed parts and other sections

of the shale surface. The Laplacian $L(x, y)$ of an image with pixel intensity values $I(x, y)$ is described in Equation 2. [Figure 1](#) and [Figure 2](#) demonstrate the original and processed images respectively.

$$L(x, y) = \frac{\partial^2 I}{\partial x^2} + \frac{\partial^2 I}{\partial y^2}$$

Detection of Shale Sections with Absorbed Moisture

The preprocessed image is now ready to be analyzed for determination of shape and percentage of water absorbed sections of the Pierre Shale. To segment the shale surface between moisturized surface (close to white) and dry part (darker sections), a threshold function is used. The threshold function illustrates the system sensitivity to moisture effects on the shale surface. Finally, as we talk about digital images and pixels in a discrete manner, the moisturized percentage of the image can be obtained with simple calculation because the threshold function results in an array of 0 and 1 representing the black and white sections, respectively. [Figure 3](#) demonstrates the final processed digital image of [Figure 2](#) for black and white image segmentation, where the moisture percentage is 13.0305% of the total.

Results

General

[Figure 4](#) demonstrates two different specimens of Pierre Shale prepared for our experiments presented in this work. They appear seemingly “dry”. However, at the same time we noticed that, as shown in [Figure 5](#), the mass of the specimen *decreased initially* when subjected to the environmental chamber humidity level which was lower than the humidity of storage area; the base humidity. To understand the behavior of Pierre Shale better, after four days of initial exposure, we increased the percent humidity of the environmental chamber above that of the humidity of the storage area. Upon weighing the specimen, we noticed, as shown in [Figure 5](#), the mass of the specimen *increased*. This gave us a clue that this particular shale is highly hygroscopic in nature and adjusts its mass by adapting to the humidity of the environment. For this reason we decided to measure the original water content of some “dummy specimens”. The original water content and mass of each dummy specimen is shown in [Table 1](#).

Comparison of J and R specimens in terms of semiquantitative bulk mineralogy and clay fraction, as shown in [Table 2](#) and [Table 3](#), clearly indicate the abundance of smectite and illite clays are responsible for strong hygroscopic nature of Pierre Shale.

Results of Scanning Electron Microscope (SEM) Imaging

As noted earlier, we selected two samples J and R for further analysis to gain a better insight into the effect of various levels of humidity on fracturing or initiating fractures in Pierre Shale. For this purpose we conducted cyclic experiments to document the variance of microfracture generation between the samples under cyclic levels (30% and 90%) of vapor pressure (humidity).

[Figure 6](#) shows SEM images of fractures in sample R at a magnification of $\times 200$. Image R1 has three fractures in an orthogonal orientation. Fractures X, Y and Z have widths of approximately 40, 35 and 20 microns respectively. The varying width of the fractures can be used to infer failure sequence: the widest fracture X appears to be the first to generate and it continued to grow, while Y (a moderately narrower fracture than X), and Z (the narrowest fracture), initiated. Accordingly, fracture Y appears to have initiated before Z. The width of the fracture in image R2 measures about 40 microns and that in image R3 about 35 microns.

The fractures are generated as a result of tensile and shear failure of the shale matrix under high water saturation. Water is first adsorbed on the shale surface due to the presence of clays. Water adsorption activates the capillaries, which results in absorption into the ultra-small pore of the shale matrix. Due to water absorption, pore pressure develops inside the capillaries until 100% saturation is achieved. Fractures initiate where capillaries absorb moisture and subsequently the pressure builds up to a point where the rock matrix can no longer withstand the tensile or shear forces, hence the shale fails. In closer examination of [Figure 6](#) we found in addition to tensile forces, shear forces also play a role in the process of adsorption-induced orthogonal fractures (image R1) and microfractures in images R2 and R3.

Studying the images further, the primary author postulated that the white surfaces, shown as C on images R1, R2 and R3, indicate locations where capillaries are the most concentrated and this is where SEM Column charging occurs. He theorized that a column of SEM will only charge where there is water, thus the SEM image could be used as a technique to identify the most susceptible areas on a shale specimen that can get saturated. The SEM images also confirm the water retention capacity of the shale capillaries suggested in [Table 1](#).

In images R2 and R3 of [Figure 6](#), the generated ultra-small fractures denoted by “m” connect the main fracture to the shale fissility planes. This phenomenon has important implications towards improving shale permeability where initially the capillaries get saturated.

[Figure 7](#) shows images of specimen J under a magnification of $\times 200$. The SEM images indicate that the specimen actually fractured upon being subjected to cyclic levels of water vapor pressure for an extended period of time. However, in contrast to specimen R, the fractures in specimen J are much smaller, measuring about 3 to 4 microns in width. Further study of specimen J, for example in image J2, we observe thread-like features on its surface indicated by S, which are absent in specimen R. The thread-like features are most likely microfractures filled with cement material due to precipitation or biological secretions. Also, O in image J2 indicates substances most likely organic matter in nature. The organic matter can provide extra cementation, in addition to precipitated cement or biologically formed cement, thus enhancing the specimen strength and resistance to tensile failure. Apparent in both images of specimen J in [Figure 7](#), are the white surfaces which have been already discussed. It can be observed that the fracture in Image J1 occurs along the white surfaces, suggesting that the fractures initiate at the fissility planes where the saturated capillaries are located and from there extend to connect with other fractures in the neighboring fissility planes.

To determine the critical surface saturation, we quantified the percent moisture necessary for fracture initiation. Following the processing methodology discussed earlier, we found a surface saturation of approximately 16.2757 percent is the critical minimum for these Pierre Shale specimens.

[Figure 9b](#) depicts the percent moisture has not reached its critical minimum value after processing and despite the presence of moisture there are no microfractures similar to that found in R specimens. As mentioned previously, the resistance of specimen J2 can be attributed to the existence of organic matter, cement precipitates, or bacterial secretions. [Figure 10](#), the XRD overlay of specimen J (blue) and R (black), clearly demonstrates the contribution of calcite (CaCO_3 peak in J) to offer resistance to fracturing or microfracture initiation is much larger for specimen J than R.

To compare the differences among various R specimens in terms of the moisture area to fracture area ratios, we followed the image analysis methodology mentioned earlier and have shown the results in [Figure 11](#), [Figure 12](#), and [Figure 13](#). It is interesting to note that the ratios in R1 and R2 images are very close to each other but the ratio in R3 is quite higher. This evidence suggests that each specimen at the end of exposure to water vapor has its own limiting capillary saturation level beyond which additional saturation may not produce more fractures or more microfractures. Now the question becomes this: if the water saturation end point is reached, does the elemental composition of Pierre Shale affect the *number* of fractures? To search for the answers we conducted SEM-EDX elemental and oxide analysis.

Results of SEM-EDX Elemental Analysis

[Table 4](#) shows some of the results elemental concentration within the area of *fracture* bounded by the square in [Figure 8a](#) and [Figure 9a](#) (J specimen), and [Figure 11a](#), [Figure 12a](#) and [Figure 13a](#) (R specimen). The concentrations are arranged in terms of mono and divalent elements.

Examination of [Table 4](#) shows the presence of higher amount oxygen in specimen J which, in addition to cements such as organic matter, calcite/aragonite (CaCO_3), and biological secretions ([Figure 10](#)) may also be responsible for generating oxide cements of Fe, Ca, Mg, K, and Na. Also, elemental substitution of one element for another could play a role in specimen J to resist fracturing, fracture widening, and propagation of microfractures. Na may be responsible for saturation and activation of Pierre Shale capillaries. Further examination of elemental concentration of Fe in specimen R may be related to formation of siderite cement (FeCO_3), ankerite [$\text{Ca.Fe}(\text{CO}_3)_2$] and/or dolomite [$\text{Ca.Mg}(\text{CO}_3)_2$] traces not detected by XRD ([Figure 10](#)) and the *number* of fractures initiating in specimen R, i.e. less siderite or iron oxide cement or any other traces of cementing material in Pierre shale the more the fractures as in R1 image ([Figure 11](#)).

Conclusions

Based on the results of this study, we conclude that:

1. Pierre Shale has extremely high capacity to retain water because of its inherently high capillary suction pressure due to high smectite clay content.

2. Fractures initiate where capillaries absorb moisture leading to internal pressure build up, which pulls apart and fractures the shale matrix.
3. Failure modes in the shale matrix are as a result of tensile and shear actions. Capillary pressure build up due to moisture absorption generate tensile fractures with displaced planes, showing shear action.
4. Scanning Electron Microscope can be used as a technique to locate the most susceptible areas of a shale sample that can get saturated. A column of SEM will only charge (indicated by white surfaces) where there is water saturation. Consequently, SEM-Column charging indicates locations where tremendous adsorption in capillaries occurs.
5. Concentration of calcite cement, cement-forming metal oxides, and organic matter strengthens the rock and increases its resistance to capillary pressure-induced tensile and shear forces. Hence, shale with higher cement-forming metal oxides and organic matter limits formation of tensile fractures.
6. The amount of absorbed water vapor is directly related to the initiation of microfractures and activation of capillaries in the shale.
7. Dynamic thresholding and segmentation parameters illustrate the robustness of image processing technique for images with dissimilar illuminations and colors.
8. The proposed technique can analyze the shale specimens automatically, quickly, and reliably.

References Cited

- Hayatdavoudi, A., M.A. Boamah, A. Tavanaei, K.G. Sawant, and F. Boukadi, 2015, Post frac gas production through shale capillary activation: University of Louisiana at Lafayette, SPE Production Operations Symposium, Oklahoma City, Oklahoma, March 1-5.
- Chitila, D., 2014, Effect of variable temperature and water vapor on fracture propagation in shale: M.S. Thesis, University of Louisiana, Lafayette.
- Savage, F., 2014, Effect of dry-wet cycles on fracture propagation in shale and gas production mechanism: M.S. Thesis, University of Louisiana, Lafayette.
- Hayatdavoudi, A, K.G. Sawant, and F. Boukadi, 2015, A chemo-physical model for predicting post-fracking pressure build-up in Pierre Shale: Proceedings of ISRM #838, Montreal, Quebec, Canada.

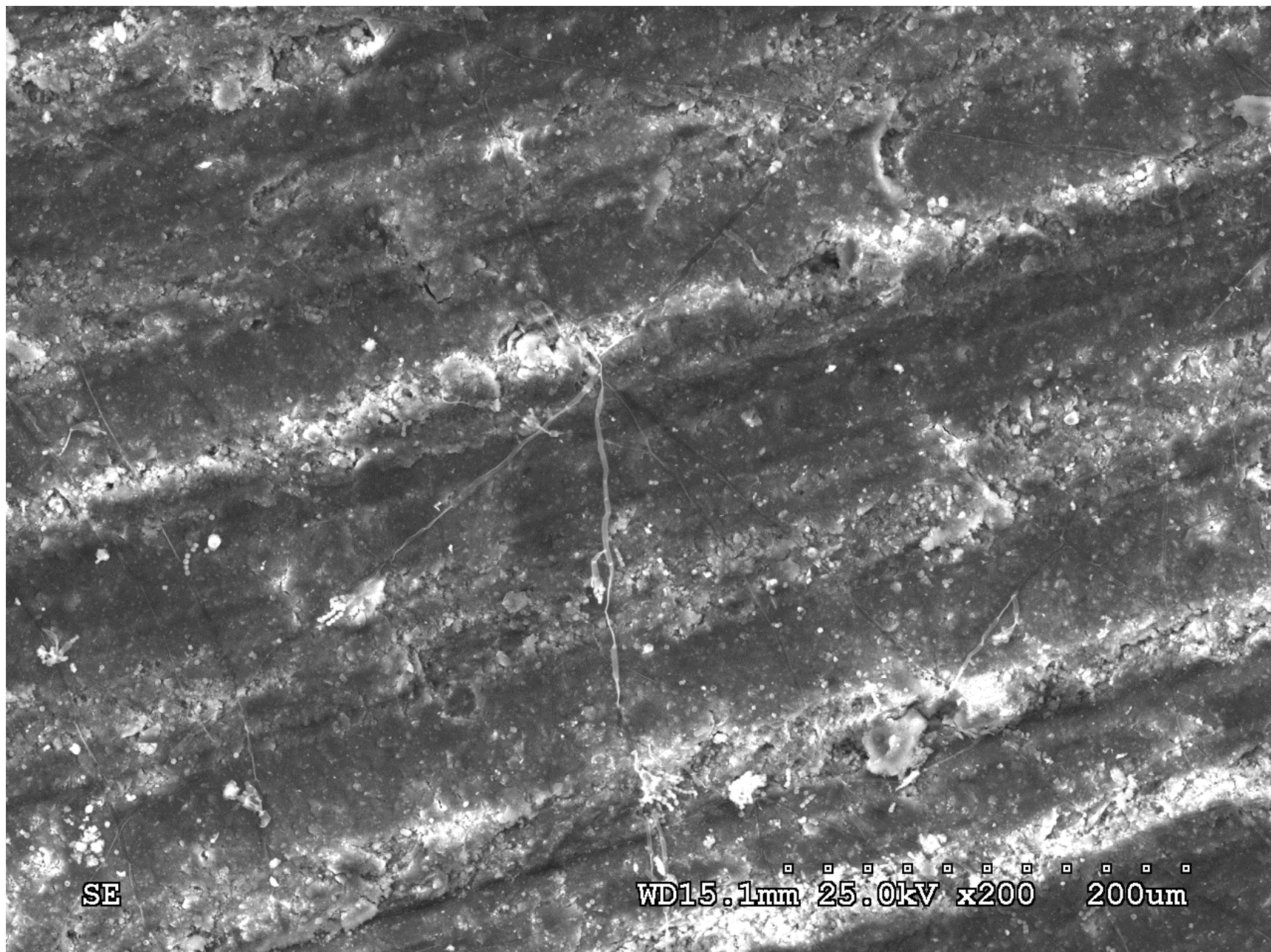


Figure 1. Original image.

Original Image Contrast

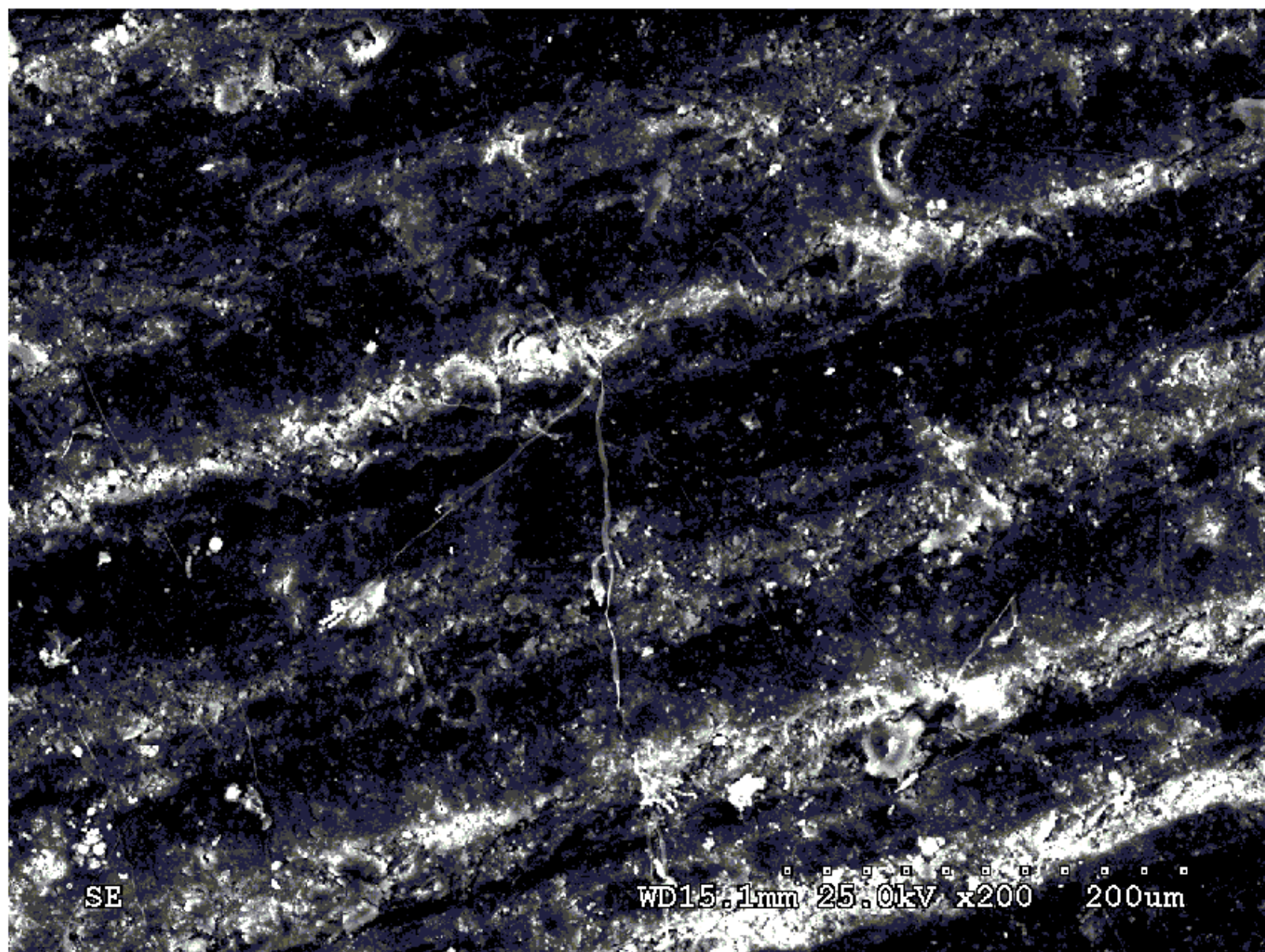


Figure 2. Processed image (contrast and edge are bold).

Moisture= 13.0305%

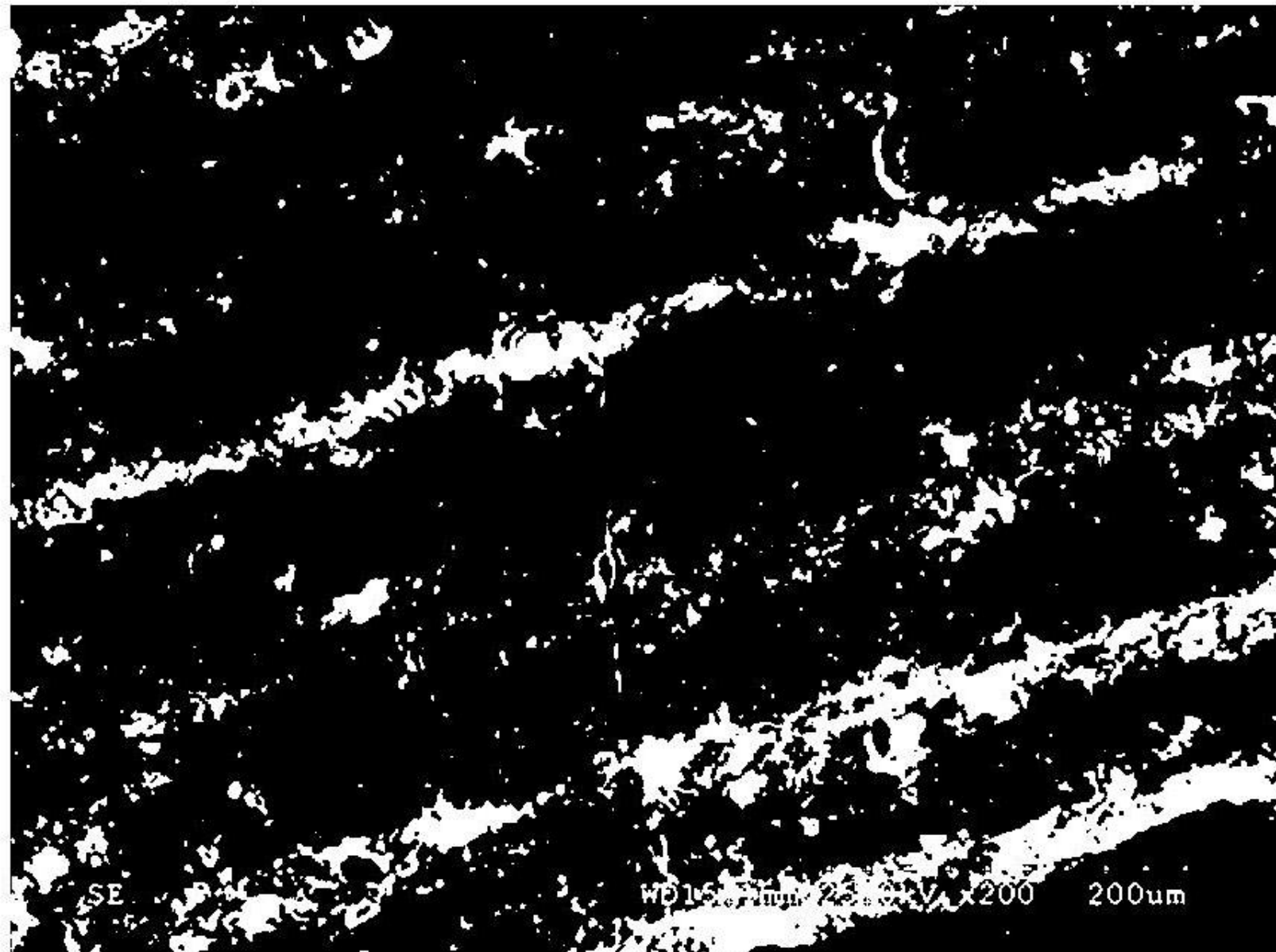


Figure 3. Segmented SEM image representing the moisturized and dry shale surfaces.



Sample J.
Dim: (7.9×5.4×8.6) mm



Sample R
Dim: (11.3×8.9×10.6) mm

Figure 4. Fresh specimens of Pierre Shale prepared for experiments.

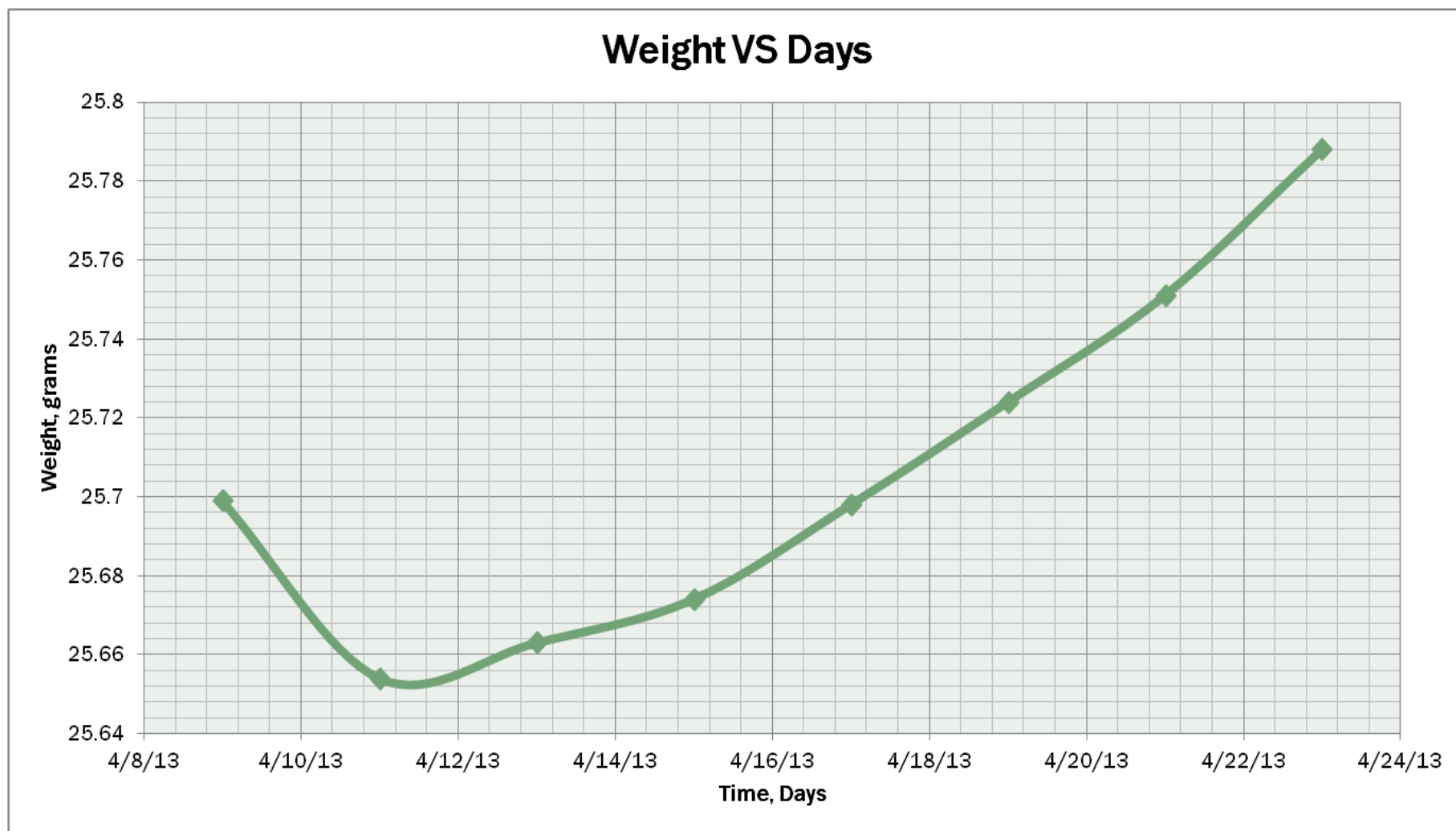


Figure 5. Pierre Shale exposed to low and high humidity (vapor pressure).

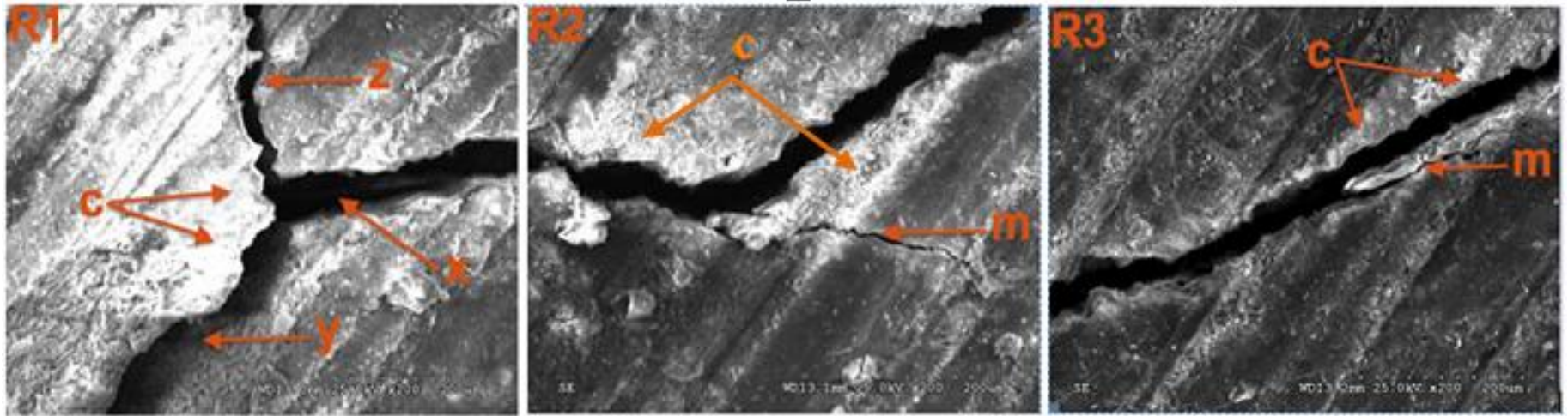


Figure 6. SEM images of specimen R1 showing (X, Y, Z) orthogonal tensile fractures with some shear displacements and in images R2 and R3 shear fractures. Letter (c) denotes SEM-column-charging surface and (m) denotes microfracture.

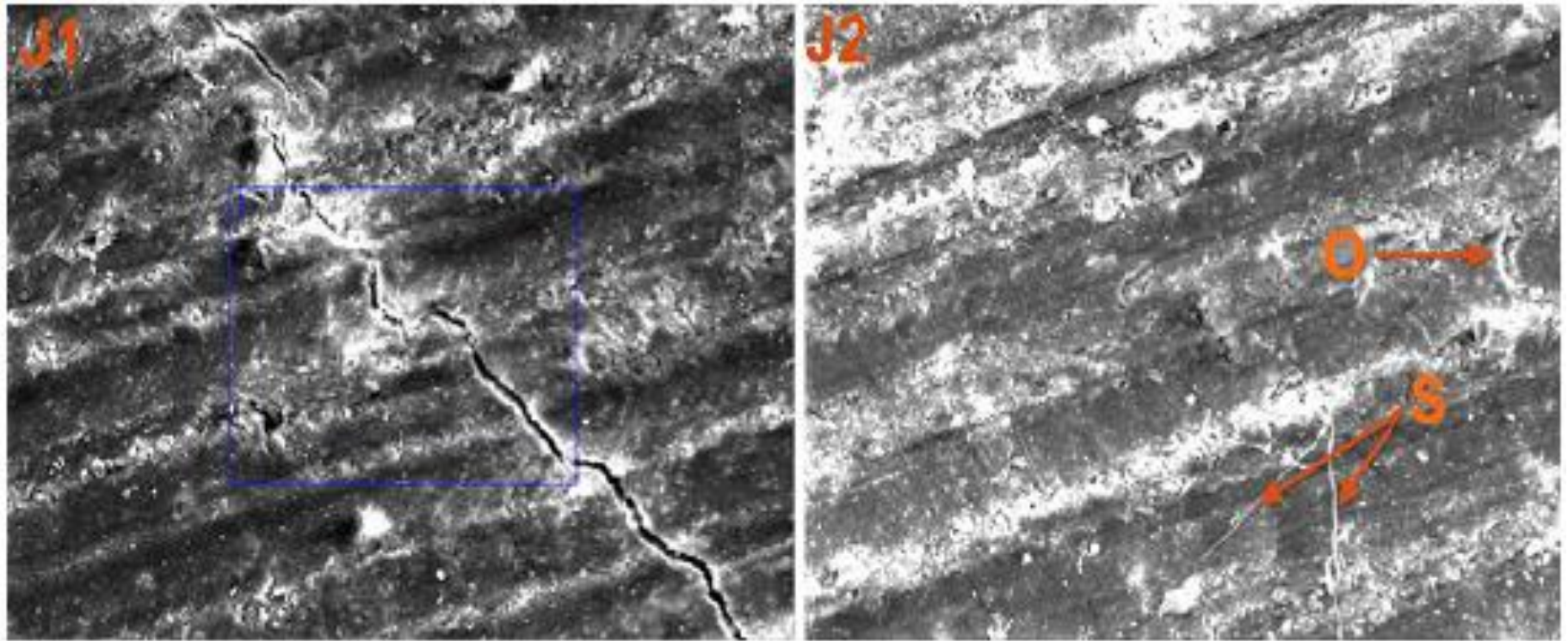
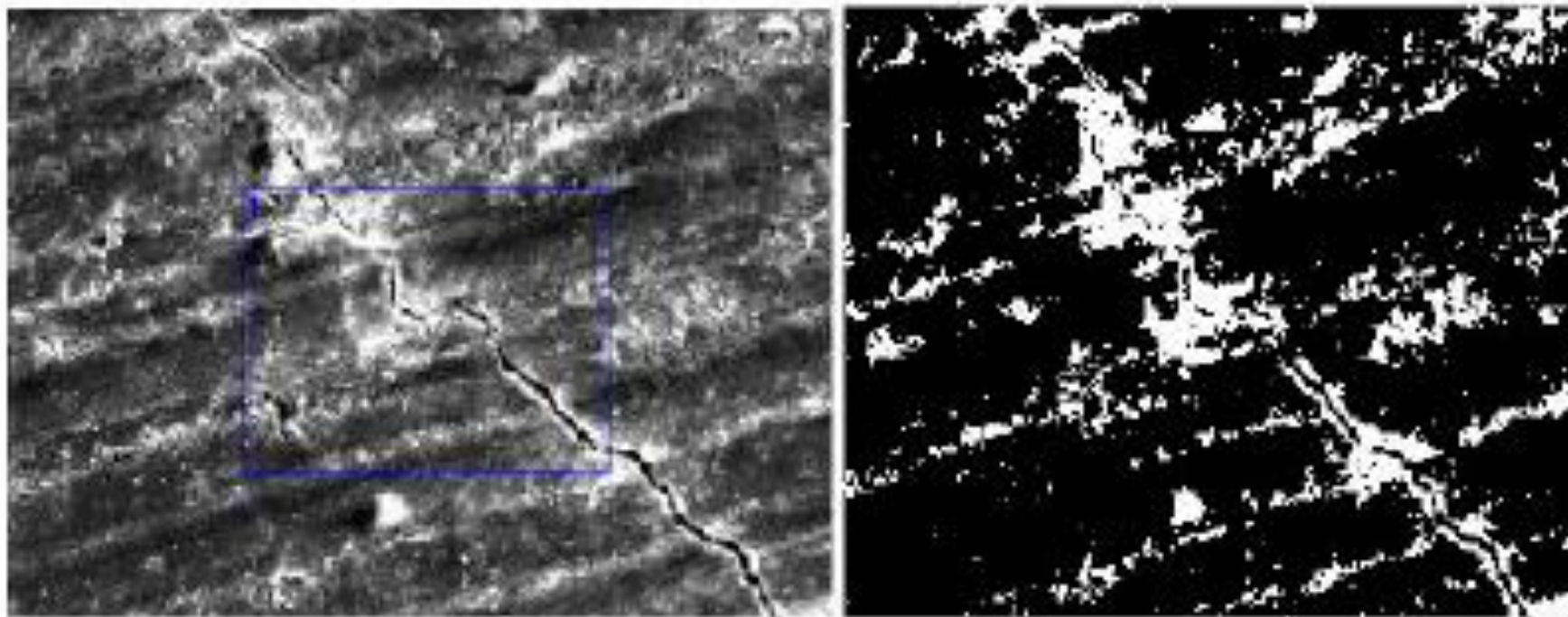


Figure 7. SEM images of specimen J. showing (o) organic matter, and (s) precipitated or biologically formed calcium carbonate.



(a)

(b)

Figure 8. (a) Preprocessed, and (b) processed (percent moisture=16.2757%) image for specimen J1.

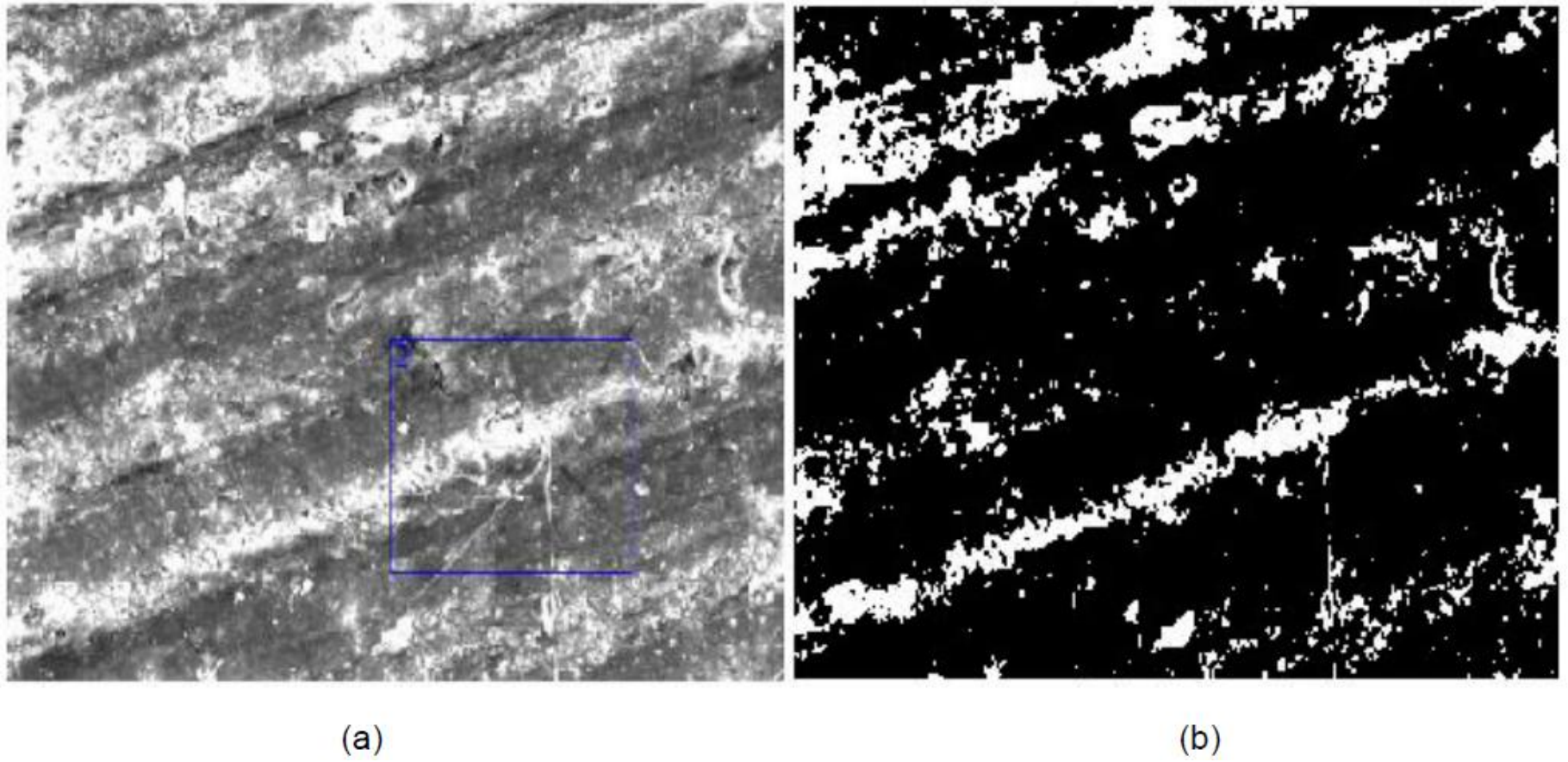


Figure 9. (a) Pre-processed, and (b) processed (percent moisture=15.8951%) image for specimen J2.

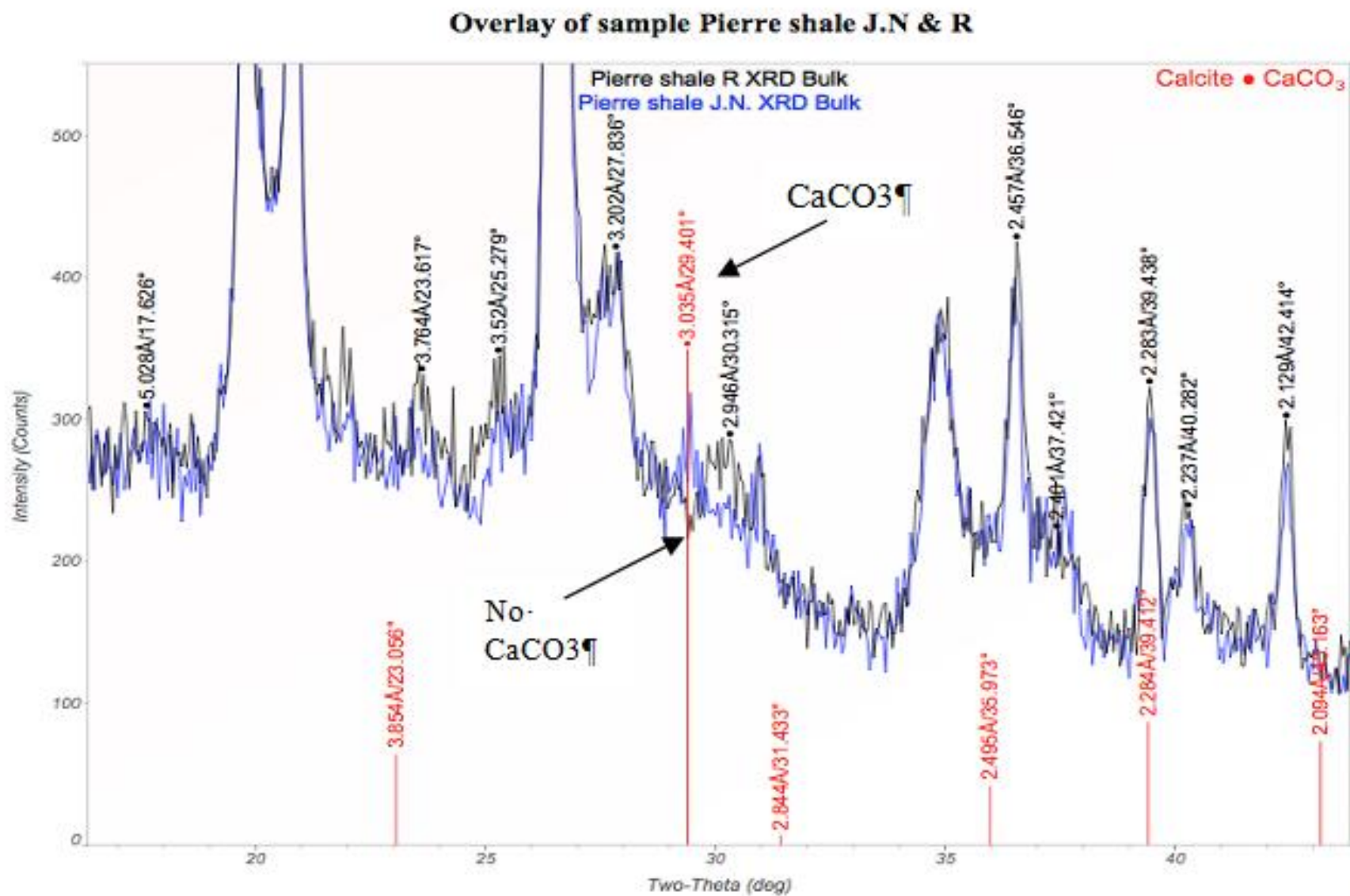


Figure 10. XRD pattern for Pierre Shale samples J and R showing calcite precipitate filling an old fracture.

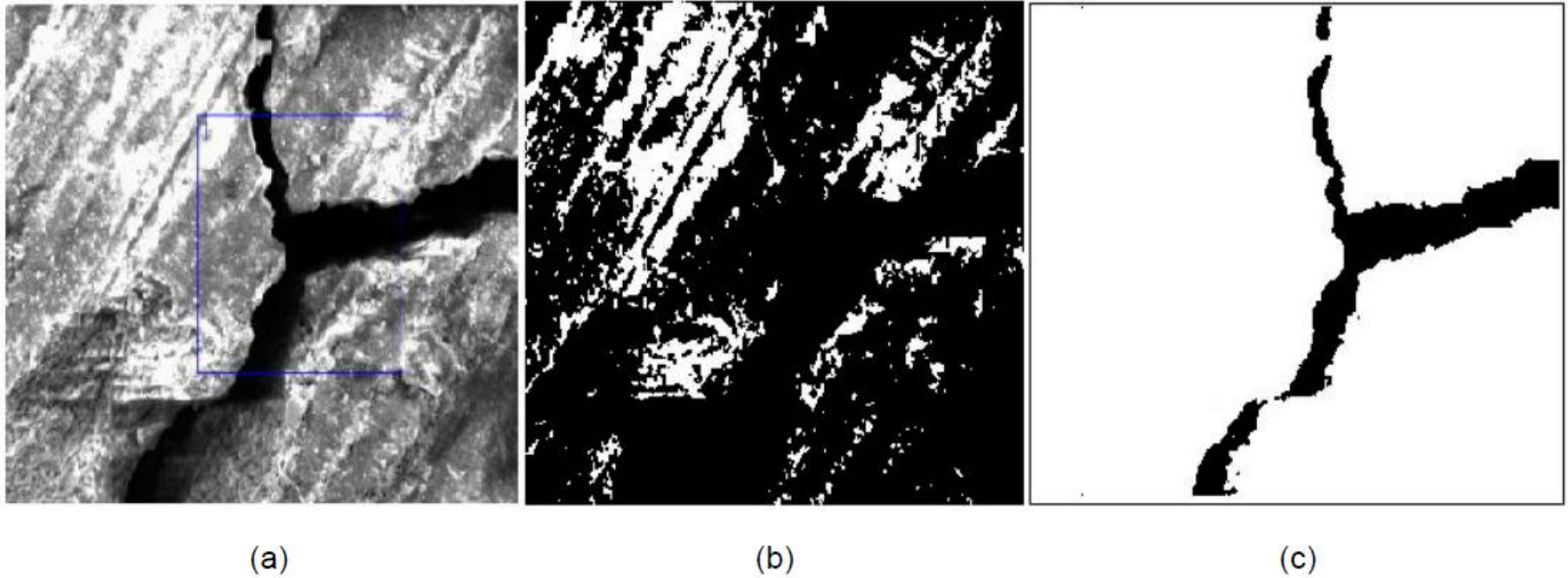


Figure 11. (a) Preprocessed, (b) processed (percent moisture=18.7279%), and (c) processed (percent fracture=8.6632%) image for specimen R1. Moisture area to fracture area ratio = 2.161.

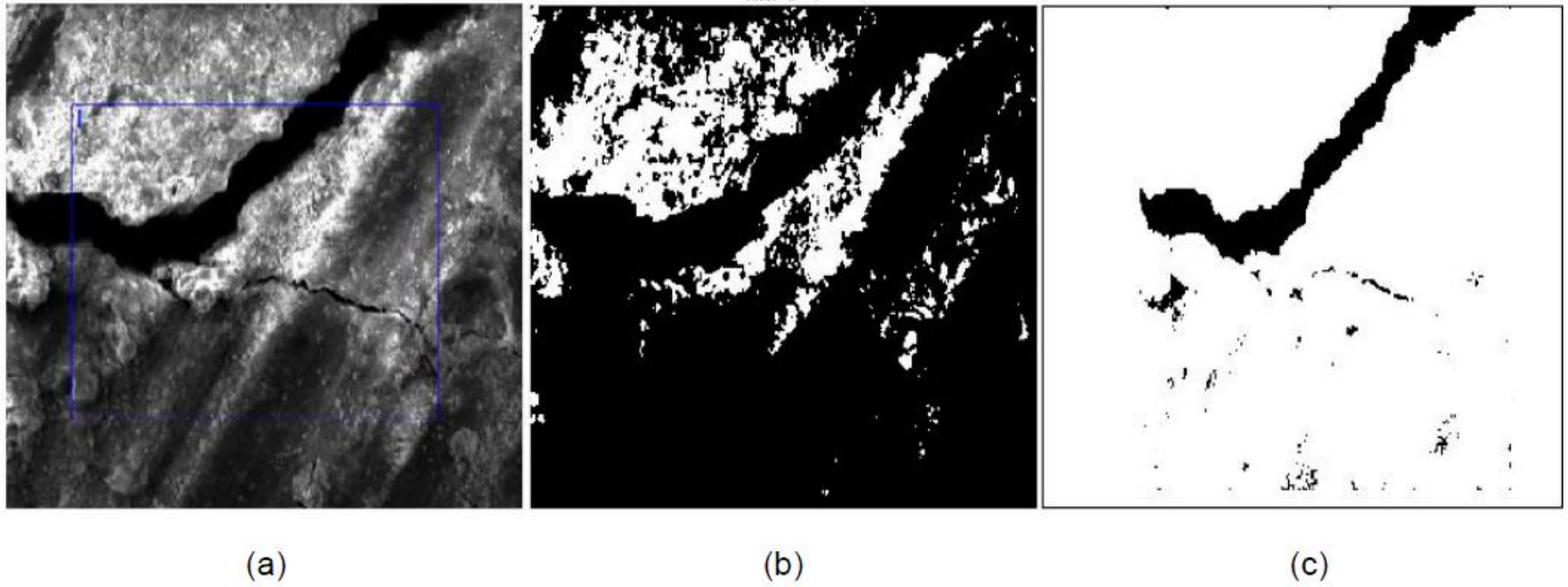


Figure 12. (a) Preprocessed, (b) processed (percent moisture=18.7347%), and (c) processed (percent fracture=8.629%) image for specimen R2. Moisture area to Fracture area ratio = 2.171.

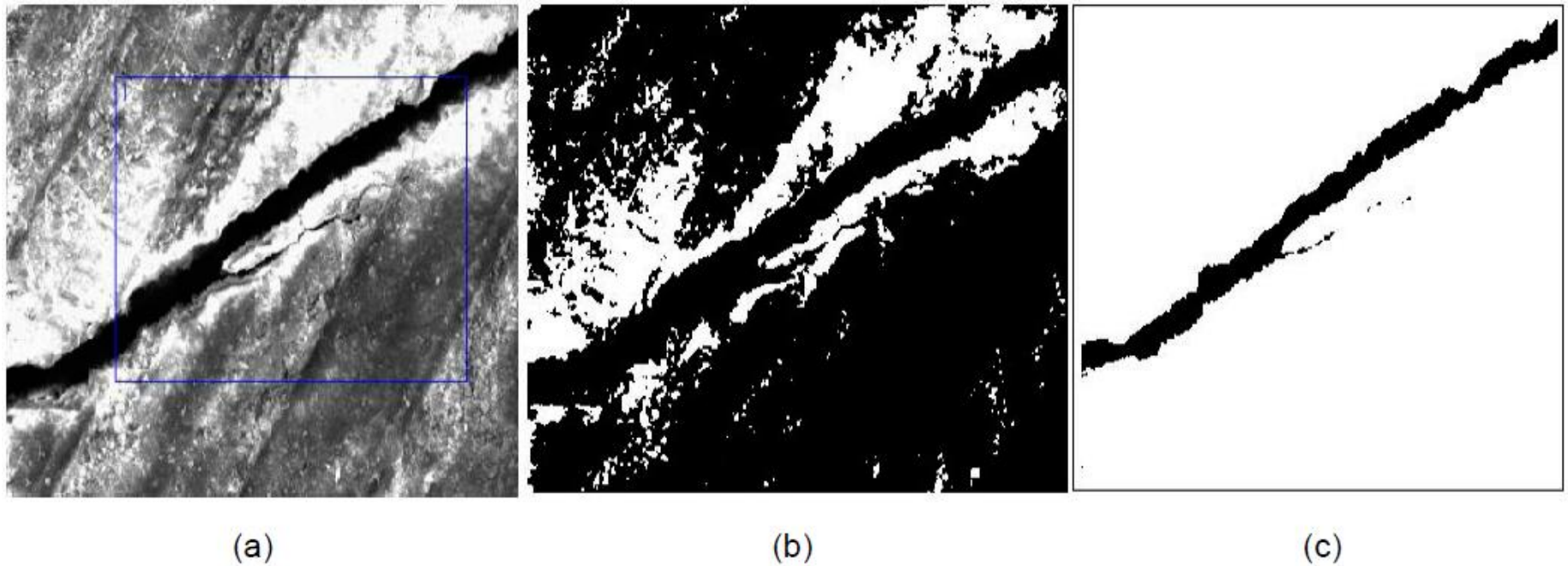


Figure 13. (a) Preprocessed, (b) processed (percent moisture=22.5642%), and (c) processed (percent fracture=6.2238%) image for sample R3. Moisture area to fracture area ratio = 3.625.

P/Po	Method	Volume of water (cm ³)	cc/g
90%	Weight difference	0.248cc	0.01
90%	Volumetric	0.24cc	0.01
90%	Weight Difference	0.222cc	0.011
90%	Volumetric	0.21cc	0.01

Table 1. Shows that the volume of water retorted from the “dummy” specimens are very close and therefore suggest that the specimens were most likely saturated with water vapor at the end of the first experiment (Savage, 2014). At this point we investigated the reason(s) for hygroscopic nature of the shale by identifying the mineral and clay content of the specimens using X-ray diffraction method.

Bulk Mineralogy		
Mineral	Sample R (wt %)	Sample J (wt %)
Quartz (SiO_2)	58	54
K-Feldspars (KAlSi_3O_8)	2	3
Plagioclase ($\text{NaAlSi}_3\text{O}_8$)	3	3
Illite ($\text{K}_{1-1.5}\text{Al}_4(\text{Si}_{7-6.5}\text{Al}_{1-1.5})\text{O}_{20}(\text{OH})_4$)	12	12
Kaolinite [$\text{Al}_4\text{Si}_4\text{O}_{10}(\text{OH})_8$]	1	0.6
Smectite $(\text{Ca},\text{Na})_{.7}(\text{Al},\text{Mg},\text{Fe})_4[(\text{Si},\text{Al})_8\text{O}_{20}](\text{OH})_4.n\text{H}_2\text{O}$	25	27

Table 2. The bulk mineral for specimens J and R.

Relative% Clay		
	Sample R (wt%)	Sample J (wt%)
Illite $(K_{1-1.5}Al_4(Si_{7-6.5}Al_{1-1.5})O_{20}(OH)_4)$	31	29
Kaolinite $[Al_4Si_4O_{10}(OH)_8]$	2	1
Smectite $(Ca,Na)_{.7}(Al,Mg,Fe)_4[(Si,Al)_8O_{20}](OH)_4.nH_2O$	67	69

Table 3. The relative clay percent in Pierre Shale.

Element	Concentration in specimens				
	J1 (Fracture)	J2 (no Fracture)	R1 (Three fractures)	R2	R3
Na	1.169	1.048	0.785	0.753	0.964
K	1.995	2.258	1.732	1.927	2.142
Mg	1.655	1.73	1.476	1.404	1.676
Ca	1.003	0.921	2.374	3.572	3.114
Fe	2.563	2.929	2.671	3.572	3.114
O	48.337	48.122	45.951	45.74	47.78

Table 4. Some results of SEM-EDX elemental analysis.